ACS APPLIED ENERGY MATERIALS

Forum Article

Cite This: ACS Appl. Energy Mater. 2019, 2, 19−28

www.acsaem.org

Evidence and Influence of Copper Vacancies in p-Type $CuGaO_2$ Mesoporous Films

Alexandria R. C. Bredar,[†] Miles D. Blanchet,[‡] Ryan B. Comes,[‡] and Byron H. Farnum*,[†]

[†]Department of Chemistry and Biochemistry and [‡]Department of Physics, Auburn University, Auburn, Alabama 36849, United States

Supporting Information

ABSTRACT: Delafossite $CuGaO_2$ nanocrystals were hydrothermally synthesized and characterized spectroscopically and electrochemically as mesoporous thin films. The nanocrystals demonstrate a preferred orientation within the film structure, as shown by enhancement of the (00*l*) peaks via two-dimensional powder X-ray diffraction. Annealing conditions of low and high temperature (i.e., 100−300 °C), with oxygen and/or argon atmospheres, were investigated, and the resulting effect on the thin film electrochemistry was measured. Cyclic voltammetry showed an increase in non-faradaic current with higher annealing temperatures and demonstrated a quasi-reversible redox feature ($E_{1/2}$ = 0.1 V vs $Fc^{+1/0}$). This feature is assigned to a Cu^{II}/Cu^{I} redox couple associated with surface defects. X-ray photoelectron and energy dispersive spectroscopies provide evidence for Cu^{II} surface defects and copper vacancies. Electrochemical impedance spectroscopy revealed that $CuGaO_2$ films were highly conductive with $\sigma \sim 10^{-5}$ Ω^{-1} cm^{-1}, consistent with a large density of hole carriers induced by copper vacancies. The significance of synthesis, film preparation, and annealing conditions on the presence of surface defects and large hole densities is discussed. The prevalence of such defects in delafossite $CuGaO_2$ is expected to have a large impact on the use of this material as a hole transport layer in solar cell architectures.

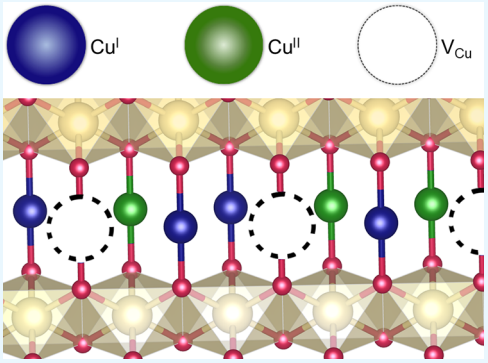

KEYWORDS: *$CuGaO_2$, delafossite, p-type metal oxide, hole transport, heterojunction solar cell*

INTRODUCTION

Delafossite $Cu^{I}M^{III}O_2$ materials have gained much attention over the past decade as p-type metal oxides capable of serving as hole transport layers (HTLs) in a wide range of heterojunction solar cells,[1−15] photocathodes for direct reduction of H^+/CO_2,[16−21] and electrocatalysts for oxidation of H_2O.[22] Interest in these materials comes from the variability of the M^{III} atom and the layered delafossite crystal structure that is known to facilitate hole (h^+) diffusion through the valence band.[23,24] For example, oxides such as $CuAlO_2$, $CuScO_2$, $CuCrO_2$, and $CuGaO_2$ are wide band gap materials that have been investigated as HTLs in combination with appropriate light absorbers and molecular catalysts to achieve solar-to-electrical[1,2,4−8,10−15] and solar-to-fuel energy conversion.[3,9] Likewise, visible band gap materials such as $CuFeO_2$, $CuRhO_2$, and $CuMnO_2$ have been shown to perform direct photocatalytic H^+/CO_2 reduction via band gap excitation.[17−21] More recently, $CuCoO_2$, $CuRhO_2$, $CuFeO_2$, $CuCrO_2$, and $CuMnO_2$ have all been shown to possess electrocatalytic properties toward water oxidation.[22]

The layered delafossite structure is also a key aspect of their scientific interest. Figure 1 shows the delafossite lattice as the 3R polymorph where alternating layers of Cu^{I} atoms and edge-shared MO_6 octahedra stack in the *c*-direction. Orbital mixing of Cu 3d and O 2p orbitals delocalizes the valence band and results in p-type conductivity. Charge transport, however, is

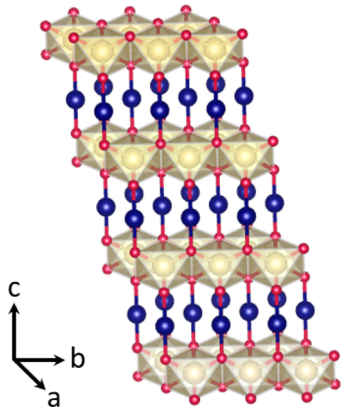

Figure 1. $CuGaO_2$ delafossite (3R) crystal structure where copper atoms (blue) lie in the *ab*-plane and stack alternately with edge-shared gallium oxide layers in the *c*-direction.

Special Issue: New Chemistry to Advance the Quest for Sustainable Solar Fuels

Received: September 14, 2018
Accepted: December 13, 2018
Published: December 27, 2018

DOI: 10.1021/acsaem.8b01558
ACS Appl. Energy Mater. 2019, 2, 19−28

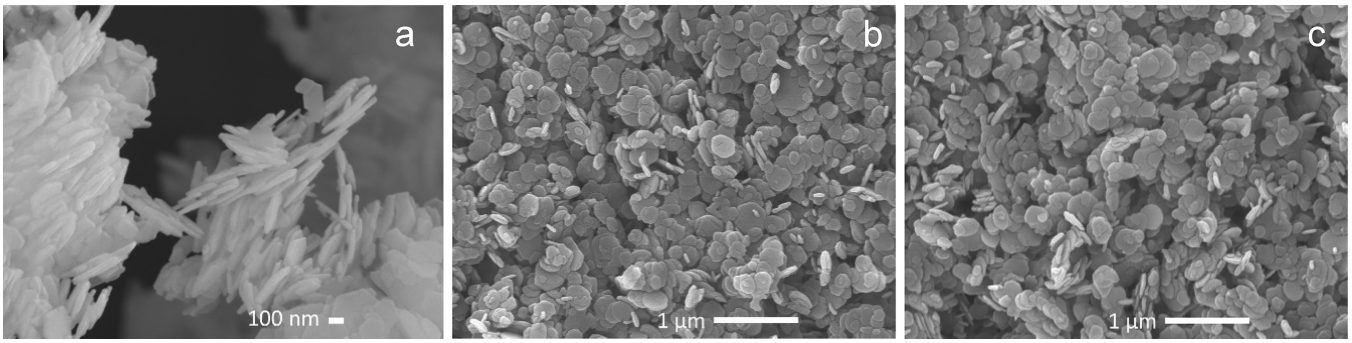

Figure 2. SEM images of $CuGaO_2$ nanocrystals: (a) powder, (b) film annealed at 200 °C O_2, and (c) film annealed at 200 °C O_2/500 °C Ar.

highly anisotropic with faster hole diffusion occurring through the Cu^I layer vs across alternating Cu^I/MO_6 layers. For example, experimental measurements have shown that the hole mobility of $CuAlO_2$ in the [100] and [010] directions is 25 times faster than transport in the [001] direction.[24]

Here we have investigated the structural and electrochemical properties of $CuGaO_2$ nanocrystalline mesoporous films in acetonitrile solution. $CuGaO_2$ has been studied previously as HTLs for dye-sensitized solar cells (DSSCs),[2,6,7,10,14,25] perovskite solar cells,[11] organic photovoltaics (OPVs),[1] and for CO_2 reduction with molecular chromophore−catalyst assemblies.[9] Previous results have noted that Mg-doping and thermal oxidation of $CuGaO_2$ can improve solar cell performance in DSSCs[2] and OPVs,[1] respectively. In these examples, improved solar cell efficiency was attributed to a greater conductivity of holes throughout the nanocrystalline films due to a larger hole density (n_{h+}). Here, we show that a large n_{h+}, induced by copper vacancies in the delafossite lattice, can result in surface defects and give rise to characteristic electrochemical features. $CuGaO_2$ films also display large conductivities on the order of 10^{-5} Ω^{-1} cm^{-1}, attributed to the high concentration of holes and a preferred orientation of nanocrystals in the film structure.

EXPERIMENTAL SECTION

Nanocrystal Synthesis. $CuGaO_2$ nanocrystals were synthesized via a hydrothermal preparation, adapted from previously reported syntheses by Popplemeier, Jobic, and Cheng.[8,10,26] Copper(II) nitrate hemipentahydrate ($Cu(NO_3)_3{\cdot}2.5H_2O$, Acros Organics, 98%+) and gallium(III) nitrate($Ga(NO_3)_3{\cdot}H_2O$, Alfa Aesar, 99.99%) (5 mmol each) were dissolved in deionized water (15 mL, 18 MΩ cm, Milli-Q). The solution was chilled in an ice bath and stirred continuously for 1 h. Ethylene glycol (5 mL, VWR) was then added to the mixture as a reducing agent, and the pH of the solution was adjusted to ∼9 using a 2.5 M KOH solution in 1 mL increments. The final solution was stirred for 1 h before transfer into a 45 mL Teflon-lined autoclave (Parr) for hydrothermal reaction at 190 °C for 24 h in a box furnace (Lindberg Blue M). The resulting particles were washed overnight with ammonium hydroxide (NH_4OH, 28 vol %, BDH) to remove CuO and Cu_2O side products and then centrifuged and washed with deionized water 3 times. The particles were finally washed with acetone and dried in a vacuum oven (Lindberg Blue M) to result in a final yield of 60%.

Film Preparation. A $CuGaO_2$ nanocrystal paste was prepared by adding deionized water (3.3 mL, 18 MΩ cm, Milli-Q), adjusted to pH 1 using nitric acid (20 μL, HNO_3, VWR, 70%), and poly(ethylene glycol) (0.25 g, PEG, MW 20,000, Millipore Sigma) to dry $CuGaO_2$ powder (0.5 g). The final composition of the paste was 15 wt % $CuGaO_2$ and 7.5 wt % PEG. The paste was sonicated using an ultrasonication horn (Branson 150) for 30 s to improve particle dispersity. $CuGaO_2$ mesoporous thin films were prepared by doctor blading the nanocrystal paste onto conductive FTO glass (SnO_2:F, 15 Ω/cm^2, Hartford Glass, Inc.). Films were then annealed in a tube furnace (Lindberg Blue M) under an oxygen atmosphere (99.999%, Airgas) at temperatures between 50 and 500 °C for 30 min (400 cm^3/min) followed by a second step under an argon atmosphere (99.999%, Airgas) at 500 °C for 30 min (400 cm^3/min).

Characterization. A range of characterization techniques were employed to study $CuGaO_2$ films before and after annealing. Attenuated total reflectance Fourier transform infrared spectroscopy (ATR-IR) was performed using a Nicolet iS-50 spectrometer with a built-in ATR. UV−vis−near-IR transmittance and reflectance spectra were collected using a Cary 5000 spectrophotometer with an integrating sphere accessory. Kubelka−Munk analysis was performed directly with the Cary Win-UV software. Scanning electron microscopy (SEM) was performed using a Jeol JSM-7000F field emission scanning electron microscope with energy dispersive spectroscopy (EDS, INCA). For a given $CuGaO_2$ film, elemental analysis using EDS was performed on three different regions with the same area (∼300 μm × 300 μm) to obtain an average and standard deviation for elemental composition. Elemental peaks were calibrated using INCA software and a copper standard. Powder X-ray diffraction (PXRD) data were collected on a Bruker D8 Discover diffractometer (Cu Kα source) with a Vantec 2000 two-dimensional area detector.

X-ray photoelectron spectroscopy was performed using a Physical Electronics (PHI) 5400 system with a monochromatic Al Kα source. High resolution scans of the O 1s, Cu 2p, and Ga 2p peaks were performed with a pass energy of 36 eV and a step size of 0.05 eV. A neutralizing electron flood gun was used to prevent charging of the samples during measurement. The Casa XPS fitting software was used for all data analysis and fitting. Voigt function peaks for each element were constrained such that the full width at half-maximum for each core-level peak was equal. The data were aligned such that the metal-oxide peak in the O 1s core level had a binding energy of 530.5 eV, which matches previous literature.[1]

Electrochemistry. Cyclic voltammetry (CV) experiments were performed with a Gamry 1010E potentiostat. Data were collected using a three-electrode setup, where the working electrode was the $CuGaO_2$ film on FTO, the counter electrode was Pt mesh, and the reference was an aqueous Ag/AgCl electrode (saturated KCl). All experimenters were performed in acetonitrile (MeCN, BDH) with 0.1 M $LiClO_4$ (99.99%, Millipore Sigma) electrolyte at a scan rate of 50 mV/s unless otherwise indicated. All reference potentials were calibrated before and after experiments using ferrocene ($Fc^{+1/0}$). The $E_{1/2}(Fc^{+1/0})$ was consistently measured to be 0.4 V vs Ag/AgCl in MeCN with 0.1 M $LiClO_4$. This value was used to adjust all potentials to the ferrocene reference.

Electrochemical impedance spectroscopy (EIS) was performed using the same potentiostat and three-electrode cell setup as the CV experiments. Data were collected over the potential range −0.9 to 1.1 V vs $Fc^{+1/0}$, with a frequency range of 250 kHz to 100 mHz with 0.1 V steps and a modulation potential of 5 mV. Data were fit using Gamry Analyst software using an equivalent circuit model described further in the text.

DOI: 10.1021/acsaem.8b01558
ACS Appl. Energy Mater. 2019, 2, 19−28

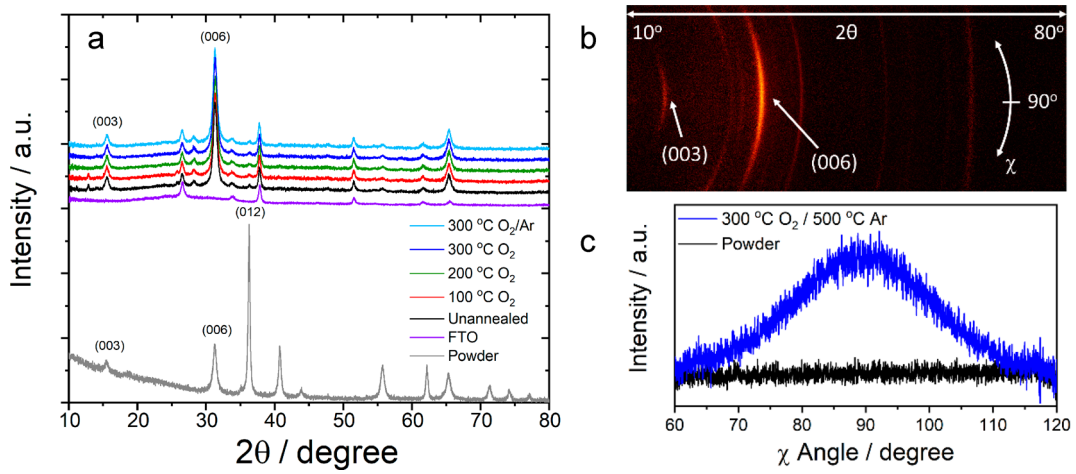

Figure 3. (a) Powder X-ray diffractograms collected for $CuGaO_2$ powder and thin films annealed over a range of temperatures and atmospheric conditions. (b) Two-dimensional ($2\theta, \chi$) XRD frame showing a preferred orientation of (003) and (006) peaks. (c) Integration of the (006) peak intensity in the χ-direction for a powder sample and a thin film annealed at 300 °C O_2/500 °C Ar.

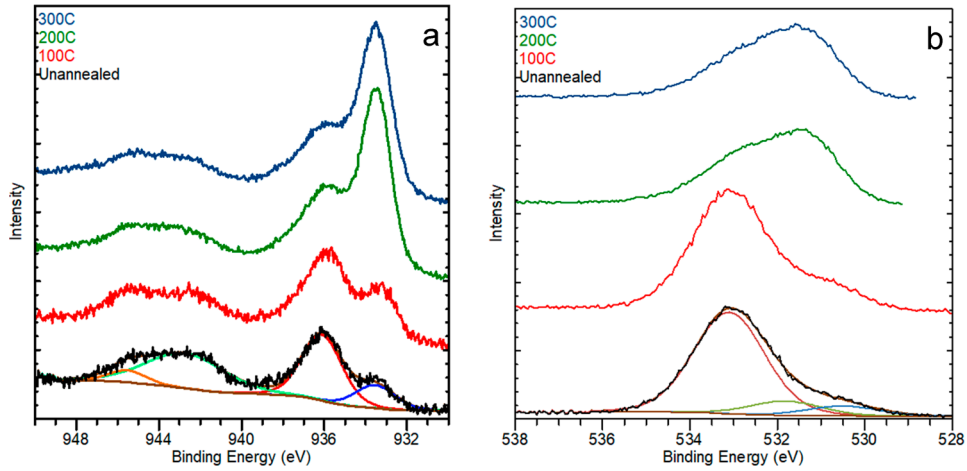

Figure 4. XPS data collected for $CuGaO_2$ films showing (a) the Cu $2p_{3/2}$ region and (b) the O 1s region as a function of annealing temperature under an O_2 atmosphere. Fitted lines indicate the location of peaks related to Cu^I (blue), Cu^{II} (red), and Cu^{II} satellites (green, orange) in the Cu $2p_{3/2}$ spectra and lattice O atoms (blue), OH_{surf} (green), and H_2O_{surf} (red) in the O 1s spectra.

RESULTS

Synthesis and Characterization. $CuGaO_2$ nanocrystals were synthesized by a hydrothermal method based on previous literature reports.[8,10,26] SEM measurements of powder samples showed nanocrystals of a plate-like morphology with widths of ~200 nm and thicknesses of ~40 nm (Figure 2). EDS measurements revealed a Cu:Ga ratio of 0.96 ± 0.02 (Supporting Information Table S1), indicating an average 4 ± 2% deficiency of copper atoms in the lattice. Nanocrystals were combined with PEG and water to form a viscous paste which was used to doctor blade 4 μm thick films onto conductive FTO glass. $CuGaO_2$ films were then annealed in a tube furnace under pure O_2 from 50 to 500 °C followed by under Ar at 500 °C. SEM images of annealed films showed no significant change in nanocrystal size or morphology with respect to powder samples.

Figure 3a shows a comparison of X-ray diffraction patterns collected for $CuGaO_2$ powder and thin film samples. The powder sample shows diffraction peaks consistent with the delafossite phase in the 3R rhombohedral polymorph.[8,10,11,26,27] Upon deposition of $CuGaO_2$ nanocrystals as a thin film, an enhancement of the (00l) peaks was clearly observed, indicating a preferred orientation of nanocrystals with the (00l) planes parallel to the FTO substrate. Panels b and c of Figure 3 show the two-dimensional XRD pattern for a thin film annealed at 300 °C O_2/500 °C Ar where higher peak intensities were centered around $\chi = 90°$. The χ angle refers to the tilt of the diffraction plane with respect to the sample stage. Films annealed under O_2 showed no change in the diffraction pattern from 50 to 450 °C. Decomposition to the oxidized $CuGa_2O_4$ spinel phase was observed at 500 °C (Figure S1). Treatment of films under an Ar environment at 500 °C showed no change in the delafossite phase.

ATR-IR experiments were performed to assess the extent of PEG removal from the thin films as a function of annealing temperature and atmospheric conditions. ATR-IR spectra of $CuGaO_2$ films showed vibrational modes associated with PEG were removed at $T \geq 200$ °C under an O_2 environment, Figure S2. Continued annealing under an Ar atmosphere at 500 °C also showed removal of PEG for films initially annealed at $T <$ 200 °C O_2.

$CuGaO_2$ films under all annealing conditions were found to exhibit high scattering of visible light, consistent with the >100 nm size of nanocrystals and 4 μm film thickness. Figure S3

DOI: 10.1021/acsaem.8b01558
ACS Appl. Energy Mater. 2019, 2, 19−28

shows UV−vis−near-IR transmittance and reflectance data of films annealed at the 200 °C O_2 and 200 °C O_2/500 °C Ar conditions where the reflectance reached a peak of 25−30% in the visible range. A Kubelka−Munk analysis of reflectance data is shown in Figure S3 where a sharp increase in the $F(R)$ function at $\lambda < 380$ nm is consistent with a wide band gap ($E_g \sim 3.3$ eV) for $CuGaO_2$, consistent with previous reports in the literature.[28]

XPS data collected in the Cu $2p_{3/2}$ and O 1s regions for $CuGaO_2$ films as a function of annealing condition are shown in Figures 4, S4, and S5. All films clearly indicated the presence of Ga^{III} (1118.5 eV), Cu^{I} (932.7 eV), and Cu^{II} (935.3 eV) at the nanocrystal surface.[1,29−31] Satellite peaks in the 940−948 eV range were also observed, typical for the presence of Cu^{II}. The Cu^{II} peak at 935.3 eV is further assigned to Cu^{II} atoms associated with surface ^{-}OH groups as opposed to lattice bound Cu^{II} atoms, which would give rise to a peak in the 933−934 eV range.[29] Furthermore, this distinction is made based on the concomitant presence of surface hydroxide (OH_{surf}) and surface water (H_2O_{surf}) detected in the O 1s region. These peaks were observed at 531.8 and 533.1 eV, respectively, with lattice bound oxygen atoms giving rise to a peak at 530.5 eV, consistent with previous literature reports.[1] Based on these assignments, unannealed films clearly contained a large amount of OH_{surf} and H_2O_{surf} molecules due to the presence of PEG and water from the doctor bladed paste. Annealing under an O_2 atmosphere is shown to remove most of these features and yield a consistent peak shape for temperatures ≥ 200 °C, which shows a main peak for lattice oxygen and shoulder peaks for OH_{surf} and H_2O_{surf}.

Integration of XPS peaks revealed changes in the Cu^{II}/Cu^{I} and Cu/Ga ratios as a function of annealing conditions, Table 1. These ratios were largest for unannealed films and decreased as the temperature increased under O_2 atmosphere. We believe the high concentration of Cu^{II} at the nanocrystal surface for unannealed films was due to stabilization by OH_{surf} and/or H_2O_{surf}. Furthermore, the total Cu/Ga ratio was greater than one for the unannealed films, suggesting possible formation of a $Cu(OH)_2$ surface layer. The decrease of Cu^{II} under oxidizing conditions was a surprising result but appears to be driven by removal of H_2O and PEG from the films at higher temperatures. Above 200 °C, Cu^{II}/Cu^{I} and Cu/Ga ratios were constant and did not change significantly when annealed further in an argon atmosphere. It is unlikely that copper atoms are completely removed from the films at these temperatures; therefore, we believe the decrease in these ratios could be due to migration of copper atoms and reduction of Cu^{II} to Cu^{I}. The average Cu/Ga ratio for all samples excluding unannealed and 100 °C O_2 was 0.5 ± 0.1. This could suggest formation of an oxidized $CuGa_2O_4$ spinel at the surface; however, we note that no lattice bound Cu^{II} peaks were detected and the Cu^{I} oxidation state is the dominant form at these conditions. Based on EDS results suggesting copper vacancies to be on the order of 4 ± 2% overall, the copper deficiency observed by XPS after high temperature annealing is believed to be due to a concentration of copper vacancies defects at the surface.

Table 1. Elemental Analysis (at. %) of $CuGaO_2$ Film Surfaces Obtained from XPS

	Cu^{I}	Cu^{II}[b]	Ga	O[c]	Cu^{II}/Cu^{I}	Cu/Ga[d]
unannealed	5.0	33.4	28.4	33.2	6.7	1.4
100 °C O_2	6.8	23.7	30.1	39.4	3.5	1.0
200 °C O_2	12.9	9.6	34.9	42.7	0.7	0.6
300 °C O_2	12.9	8.6	36.2	42.2	0.7	0.6
100 °C O_2/Ar[a]	19.7	1.1	39.7	39.4	0.1	0.5
200 °C O_2/Ar[a]	16.3	2.1	41.2	40.5	0.1	0.4
300 °C O_2/Ar[a]	11.1	6.3	36.1	46.5	0.6	0.5

[a]Ar refers to annealing at 500 °C Ar after the O_2 step. [b]Includes integration of 935.3 and 940−948 eV peaks. [c]Includes integration of only 530.5 eV peak. [d]Cu = (Cu^{I} + Cu^{II}).

Electrochemistry. Electrochemical analysis of $CuGaO_2$ films was performed using CV and EIS in acetonitrile (MeCN) solvent. In all cases, the $CuGaO_2$ films deposited on conductive FTO glass were used as the working electrode in a three-electrode setup with 0.1 M $LiClO_4$ electrolyte.

Figure 5 shows a comparison of CV data measured for films annealed at 100 °C O_2 and 300 °C O_2 followed by 500 °C Ar. Two observations of these data are readily evident. First, films annealed at 100 °C O_2 exhibited a small non-faradaic current (~5 μA) compared to 300 °C O_2 (~100 μA). A closer investigation revealed a dramatic increase in non-faradaic current as the annealing temperature jumped from 175 to 200 °C under O_2 atmosphere (Figure S6). This large change in background current is assigned to removal of the PEG polymer from the film structure, thus causing an increase in the internal surface area of the $CuGaO_2$ electrode. Second, films annealed under all conditions displayed a quasi-reversible redox feature with $E_{1/2} \sim 0.1$ V vs $Fc^{+1/0}$ followed by an irreversible oxidation near 0.8 V. The quasi-reversible feature can be seen most clearly for the 100 °C O_2 sample in Figure 5a (inset). However, as the annealing temperature was increased, the magnitude of the non-faradaic background made it more difficult to directly observe this feature. The second annealing step at 500 °C Ar was found to increase current associated with both redox features while the non-faradaic current remained nearly constant.

Electrochemical impedance spectroscopy was used to help further characterize the electrochemical properties of $CuGaO_2$ films. This technique is especially useful for differentiating multiple features such as double layer charging, charge transfer at the solid/solution interface, and charge transport through mesoporous films based on their frequency dependent responses.[32−34] EIS data were collected over a range of applied potentials from −0.9 to 1.1 V vs $Fc^{+1/0}$ with a voltage modulation amplitude of 5 mV. The modulation frequency was varied from 250 kHz to 100 mHz. From these data, the diffusion resistance and $CuGaO_2$ film capacitance can be isolated and measured as a function of applied potential and annealing conditions.

Figure 6 shows a comparison of Nyquist and Bode-phase plots obtained at an applied potential of 0 V as a function of annealing conditions. EIS data collected over all applied potentials and annealing conditions are shown in the Supporting Information. Nyquist plots display the imaginary (Z_{Im}) and real (Z_{Re}) components of the frequency dependent total impedance (Z), while the Bode-phase plots display the phase angle defined by the expression $\theta = \tan^{-1}(Z_{Im}/Z_{Re})$. Multiple arcs can be observed in the Nyquist plots for any given annealing condition, corresponding with multiple peaks in the Bode-phase plots. These arcs are indicative of distinct solid/liquid or solid/solid interfaces within the working electrode such as $CuGaO_2$/electrolyte and FTO/$CuGaO_2$.

DOI: 10.1021/acsaem.8b01558
ACS Appl. Energy Mater. 2019, 2, 19−28

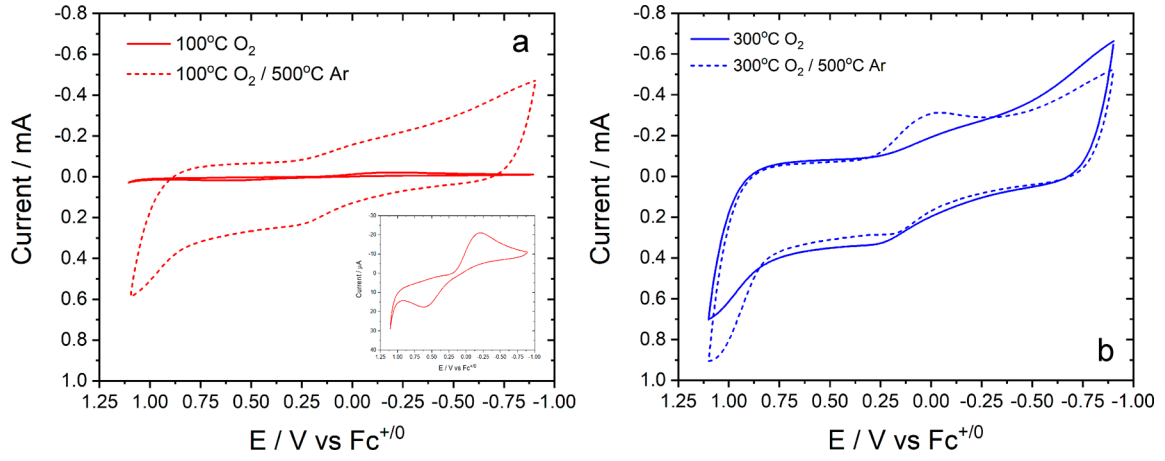

Figure 5. CV data of $CuGaO_2$ films measured in MeCN with 0.1 M $LiClO_4$ at a scan rate of 50 mV/s: (a) 100 °C O_2; (b) 300 °C O_2.

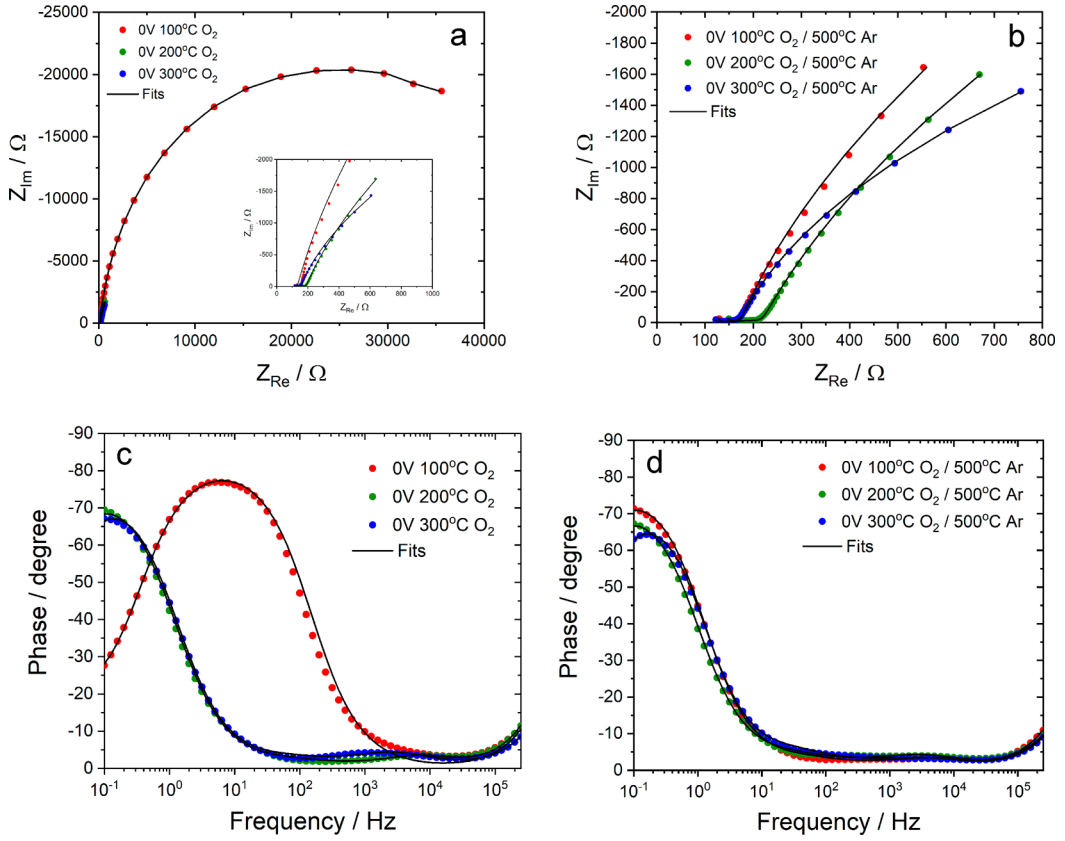

Figure 6. Nyquist (a, b) and Bode-phase (c, d) plots for $CuGaO_2$ films measured in MeCN with 0.1 M $LiClO_4$. Applied potentials are referenced to ferrocene. Overlaid fits were generated using the equivalent circuit models shown in Figure 7a and Figure S7.

EIS data were fit to the equivalent circuit model shown in Figure 7a to extract quantitative values for the interfacial charge transfer resistances and capacitances. This model has been used previously to describe EIS data collected for mesoporous metal oxides films including $CuGaO_2$. The model features a transmission line circuit element developed by Bisquert to describe both the metal oxide/electrolyte interface (R_{film}/C_{film}) and charge diffusion (R_d) as distributed elements throughout the nanocrystalline film.[33,34] A contact resistance (R_{con}) was also included to describe the resistance for charge transfer across the FTO/$CuGaO_2$ interface. The FTO/electrolyte interface was modeled as a single capacitor in parallel with the $CuGaO_2$/electrolyte interface since current may be passed through either surface. A series resistor (R_s) and a parallel R_0C_0 element were used to account for resistive losses in the external circuit and the interface of the electrolyte and reference/counter electrodes, respectively. Further details related to this model are given in the Supporting Information.

All capacitors were modeled as constant phase elements (CPE) to account for nonideality using the expression $Z_{CPE} = 1/(Q(i\omega)^{\beta})$, where Q has units of F $s^{\beta-1}$, ω is the angular modulation frequency ($2\pi f$), and β is an ideality factor which ranges from 1 to 0, with 1 representing an ideal capacitor. Ideality factors from the fitting analysis were found to be $\beta_{ref} = 0.95 \pm 0.03$, $\beta_{FTO} = 0.86 \pm 0.05$, and $\beta_{film} = 0.90 \pm 0.01$. Based on these values, the magnitude of Q was treated directly as the

DOI: 10.1021/acsaem.8b01558
ACS Appl. Energy Mater. 2019, 2, 19−28

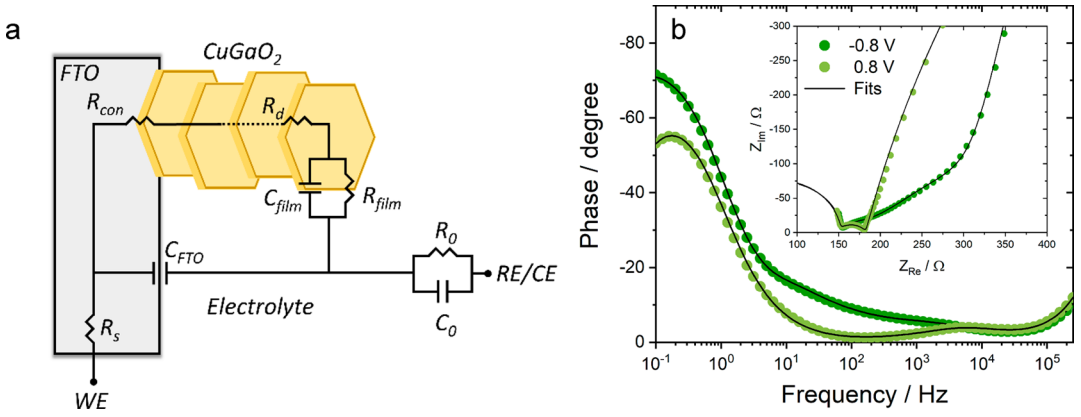

Figure 7. (a) Equivalent circuit model used to fit EIS data. (b) Bode-phase and Nyquist (inset) plots for 200 °C O_2 film for two different applied potentials. The overlaid fits highlight the effect of R_d and R_{con} on the fitting analysis.

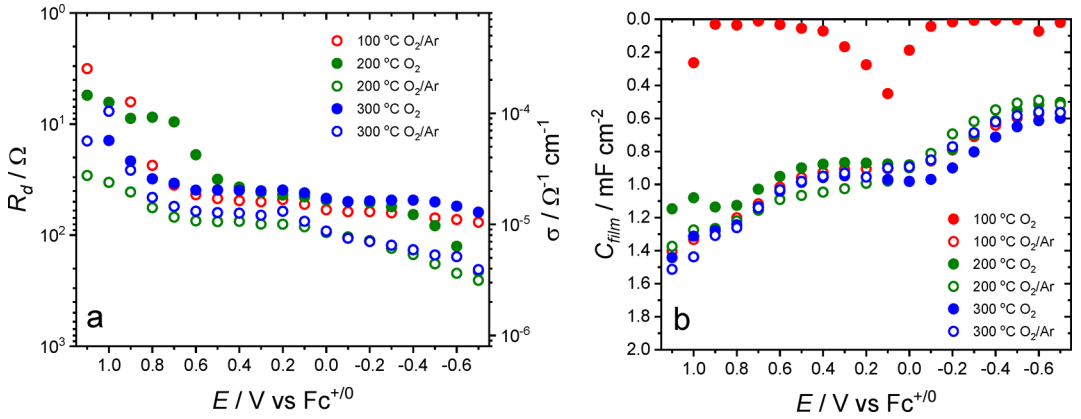

Figure 8. (a) Diffusional resistance (R_d) and (b) $CuGaO_2$/electrolyte interfacial capacitance (C_{film}) obtained from EIS modeling plotted as a function of applied potential. Capacitances were normalized to the 1 cm^2 geometric area of the $CuGaO_2$ films.

magnitude of the capacitance for each respective interface. All annealing conditions were found to fit the equivalent circuit shown in Figure 7a except for 100 °C O_2. This sample was best fit to a simplified model which substituted the transmission line circuit element with a simple parallel *RC* circuit to model the $CuGaO_2$/electrolyte interface, Figure S7. Summary tables showing fitting constants for all measured data are given in the Supporting Information.

Figure 7b shows EIS data for the 200 °C O_2 annealing condition as a function of applied potential. Overlaid lines represent fits from the equivalent circuit which highlight certain aspects of the model at different frequency regions. The high frequency feature (>10^5 Hz) was modeled by the parallel R_0C_0 circuit element and was found to be invariant from sample to sample with $R_0 = 124 \pm 21$ Ω and $C_0 = 1.2 \pm 0.4$ nF. The mid-frequency feature (10^1–10^4 Hz) was characteristic of R_d, R_{con}, and C_{FTO}. Here, the diffusion resistance R_d was modeled by the stretched tail feature shown in the Bode-phase plot and linear region between 200 and 300 Ω in the Nyquist plot at −0.8 V. As the potential was stepped positive, the magnitude of R_d decreased as shown for the 0.8 V data. This decrease is consistent with $CuGaO_2$ behaving as a p-type material where the density of hole carriers was increased at more positive potentials, resulting in a smaller diffusion resistance. Figure 8a shows a plot of R_d as a function of applied potential for different annealing conditions. Overall, the magnitude of R_d was similar across annealing conditions and decreased from ∼100 Ω to ∼10 Ω over a 1.8 V range in applied potential.

The parallel combination of R_{con} and C_{FTO} yielded a peak feature near 10^4 Hz in the Bode-phase plot of Figure 7. This feature was difficult to directly observe when R_d was large but was more easily identified at positive applied potentials when R_d was smaller. The magnitude of the contact resistance was constant ($R_{con} = 23 \pm 7$ Ω) and invariant with applied potential for all annealing conditions except for 100 °C O_2. This condition instead showed an extremely large R_{con} > 10,000 Ω which varied as a function of applied potential, Figure S8. This resistance resulted in the large peak feature observed in Figure 6c around 10^1 Hz. The large R_{con} values were assigned to a combination of incomplete sintering of nanocrystals to the FTO surface and the remaining presence of PEG inside the film pores. Poor contact at the $CuGaO_2$/FTO interface for 100 °C O_2 samples was also observed by delamination of the film after extended electrochemical experiments. The capacitance of the FTO/electrolyte interface was found to be constant over all samples with $C_{FTO} = 11 \pm 4$ $\mu F\ cm^{-2}$, consistent with other estimates from the literature.[25]

Finally, the high frequency range (>10^1 Hz) was modeled by the $CuGaO_2$/electrolyte interface represented by the parallel $R_{film}C_{film}$ component of the transmission line circuit element. Due to the fact that no electroactive species were present in solution, R_{film} was always greater than 1000 Ω, Figure S8. A plot of C_{film} as a function of applied potential for different annealing conditions is shown in Figure 8b. For the 100 °C O_2

DOI: 10.1021/acsaem.8b01558
ACS Appl. Energy Mater. 2019, 2, 19−28

film, the capacitance displayed a peaked feature near 0.1 V vs $Fc^{+/0}$, similar to the quasi-reversible feature observed from cyclic voltammetry. All other annealing conditions displayed capacitance curves that were nearly identical to each other, showing a relatively large capacitance (~0.5 mF cm^{-2}) at the negative limit of applied potentials with a nominal increase to ~1.5 mF cm^{-2} at positive potentials. A small peak in the capacitance was reproducibly observed near 0 V, again matching the observations from CV data.

DISCUSSION

Delafossite $CuGaO_2$ nanocrystals were synthesized as hexagonal plates ~200 nm wide and ~40 nm thick. This anisotropic morphology is commonly observed for delafossites and is a consequence of their layered crystal structure.[8,35] The large difference in width and thickness results in stacking of adjacent nanocrystals in the *c*-direction, as observed by SEM. Dispersion of nanocrystals into a thin film structure shows an enhancement of this stacking feature, indicating a preferred orientation of nanocrystals with respect to the FTO substrate. This is supported by SEM as well as two-dimensional XRD data where diffractions from the (003) and (006) planes were greatly enhanced upon thin film deposition. Furthermore, integration of the two-dimensional (006) peak with respect to the χ-direction shows that nanocrystals were relatively flat (i.e., parallel with the FTO substrate) with signal intensity peaking at 90°.

It is possible that the polymer present in the film upon deposition could be directing the orientation of nanocrystals. Incorporation of polymer additives such as PEG, ethyl cellulose, and terpineol to nanocrystal suspensions is a standard method of controlling particle dispersion and increasing porosity for a wide range of mesoporous metal oxide films.[5,7,36,37] However, based on the morphology of $CuGaO_2$ nanocrystals and the SEM images of powder samples which also show particle stacking, we believe the high orientation within thin films to be mostly controlled by the nanocrystalline dimensions. Indeed, other studies of $CuGaO_2$ films in the literature have also suggested oriented stacking from SEM,[10,11] yet here we show this behavior more clearly via two-dimensional powder XRD measurements.

The electrochemistry of $CuGaO_2$ films can reveal a great deal of information about its capacitance and conductivity. These two terms are important in the context of solar energy conversion as $CuGaO_2$ is used as a hole transport layer in many solar cell architectures.[1,2,6,7,10,11,14] The capacitance of the film in the region of the valence band is indicative of its ability to accept photogenerated holes, while the conductivity is a measure of how quickly those holes may be transported to the external circuit. Capacitance measurements can also yield information about defect states present at the surface of $CuGaO_2$ nanocrystals.

In the present data, CV experiments revealed a quasi-reversible redox feature at 0.1 V vs $Fc^{+1/0}$ which was supported by a capacitance peak near 0 V obtained from EIS data. A similar quasi-reversible feature in the range of 0 to 0.4 V vs SCE (−0.39 to 0.01 V vs $Fc^{+/0}$) has been observed for CuO supercapacitors and has been assigned to a Cu^{II}/Cu^{I} redox couple involving surface hydroxides.[29−31] We believe the quasi-reversible feature observed here for $CuGaO_2$ electrodes is also due to a Cu^{II}/Cu^{I} redox couple facilitated by Cu^{II} surface defects in contact with hydroxides at the nanocrystal surface. The presence of such defects is supported by XPS measurements where the largest fraction of Cu^{II} surface defects observed for annealed $CuGaO_2$ films was for the 100 °C O_2 condition. This condition also showed the most prominent quasi-reversible feature in CV measurements.

The conductivity of $CuGaO_2$ films could be estimated from the diffusion resistance (R_d) measured by EIS using the expression $\sigma = L/(R_d A(1-p))$, where σ is conductivity (Ω^{-1} cm^{-1}), L is the film thickness (cm), A is the geometric area of the film (cm^2), and p is porosity.[25,33] Figure 8a shows conductivities calculated using $L = 4 \times 10^{-4}$ cm, $A = 1$ cm^2, and the basic assumption of $p = 0.5$. The magnitude of conductivities for all samples (excluding 100 °C O_2) generally fell around 10^{-5} Ω^{-1} cm^{-1} and showed a mild increase as the applied potential was shifted in a positive direction over a 1.8 V window. These data are in contrast with a study by Giménez which showed that the conductivity of $CuGaO_2$ films measured by EIS varied from 10^{-7} to 10^{-6} Ω^{-1} cm^{-1} over a 1 V range in applied potentials.[25] Magnesium-doping, (1%)Mg:$CuGaO_2$, was found to improve the conductivity overall but still varied over an order of magnitude from 10^{-6} to 10^{-5} Ω^{-1} cm^{-1} over the same potential range. Aliovalent doping increases the density of holes (n_{h+}) and improves the conductivity according to the expression $\sigma = q n_{h+} \mu_{h+}$, where q is the elementary charge and μ_{h+} is the effective hole mobility through the mesoporous film. Large changes in conductivity with applied potential are a clear indication of electrochemical oxidation of valence band states by increasing n_{h+}. In the present study, the increase in conductivity with positive applied potentials is consistent with $CuGaO_2$ being a p-type material; however, the small change in magnitude over a wide voltage range suggests that a large density of holes is already present within the oxide, thus limiting its capacity to increase n_{h+} further.

Hsu has also shown that chemical oxidation of $CuGaO_2$ films in the presence of UV/ozone can result in higher n_{h+} and thus higher σ.[1] Here, the difference in conductivity between O_2 and Ar annealing steps also suggests that the hole density may be marginally affected by annealing conditions. XPS data show a small reduction in the ratio of Cu^{II}:Cu^{I} peaks under Ar, and in general, films annealed under O_2 are slightly more conductive than films annealed under the second Ar step. However, the effect is again relatively small with conductivity only changing by a factor of 3 for the 300 °C O_2 films measured at −0.4 V.

The high conductivity of $CuGaO_2$ films may also be aided by the preferred orientation of the nanocrystals on the FTO substrate. Stacking of nanocrystals could improve the degree of interparticle contacts, especially in such anisotropic structures, and lead to a reduction of carrier scattering at $CuGaO_2$/$CuGaO_2$ interfaces. This affect has been observed previously for mesoscale NiO nanocrystals that also adopt hexagonal nanoplate structures.[38] Delafossites are known to possess large hole mobilities; however, mobility in the [100] and [010] directions (i.e., the copper plane) is much faster than in the [001] direction.[24] The orientation of nanocrystals in the $CuGaO_2$ film indicates that charge diffusion must occur in the [001] direction to be measured by the external circuit. Therefore, particle stacking may be helping to improve the effective hole mobility in this direction.

The origin of a large hole density in the present study is believed to be due to the presence of copper vacancies (V_{Cu}) and/or interstitial oxygen atoms (O_i) in the delafossite lattice.[39,40] When either of these defects is present, a hole must be introduced to compensate charge. Most likely, this

DOI: 10.1021/acsaem.8b01558
ACS Appl. Energy Mater. 2019, 2, 19−28

hole takes the form of a Cu^{II} atom in the lattice. EDS results for $CuGaO_2$ films studied here revealed a copper deficiency on the order of 4 ± 2% overall while XPS results showed this deficiency to be on the order of 50% at the surface. Copper vacancies have been observed previously in Mg-doped $CuGaO_2$ and have been estimated to have a low energy of formation for the delafossite structure based on theoretical calculations.[2,41] Interstitial oxygen atoms in the delafossite lattice could also play a role in p-type conductivity. Defects of this type are most prominent when the M^{III} atom is larger than Sc^{III}, while smaller cations such as Al^{III} limit their formation due to a small *a*-lattice parameter.[39,42−45] Unique phases incorporating interstitial oxygens have even been observed in the case of $CuLaO_{2.66}$ and other lanthanides. The mild dependence of conductivity with O_2 annealing suggests that O_i defects may be present in $CuGaO_2$; however, a larger change in conductivity would be expected if they were the main defect type. Determining the percentage of such defects is also difficult due to the known presence of OH_{surf} and H_2O_{surf} molecules which cloud the exact determination of oxygen content in the lattice via XPS.

Assuming only copper vacancies contribute to the density of holes, we can estimate $n_{h+} \sim 10^{21}$ cm^{-3} based on the 4% estimate for V_{Cu}, the density of copper atoms in $CuGaO_2$, and assuming a 1:1 V_{Cu}:h^+ ratio. This value is on the order of electron densities found in n-type transparent conductive oxides such as Sn:In_2O_3 (ITO) and F:SnO_2 (FTO) and large enough to explain the high conductivities observed here.[46] Indeed, copper delafossites such as $CuAlO_2$ and $CuGaO_2$ have been touted as p-type transparent conductive oxides themselves.[28,47,48] Given the large hole density induced by copper vacancies, it is likely that the Fermi level of the present $CuGaO_2$ films is pinned with respect to the valence band edge. The flat-band potential (E_{fb}) of $CuGaO_2$ has been measured by Jobic at 0.49 V vs SCE in water with 0.1 M $LiClO_4$.[6] Conversion of this value to the ferrocene reference in MeCN yields E_{fb} = 0.10 V vs $Fc^{+1/0}$.[49] If the initial hole density were small, the capacitance of $CuGaO_2$ films would be expected to be large for E > 0.1 V and very small at E < 0.1 V (i.e., in the band gap). The present data instead show a nearly uniform capacitance across all measured potentials as seen in both CV and EIS data. The capacitance at E < 0.1 V was also significant with $C_{film} \sim 0.5$ mF cm^{-2}. These data collectively point to a material which is more metallic than semiconductive with behavior that is similar to that of mesoporous transparent conductive oxides.

The origin of copper vacancies in $CuGaO_2$ nanocrystals is believed to be related to the synthetic conditions for their preparation. Multiple studies have shown that solution pH is one of the largest factors controlling the growth of $CuGaO_2$ nanocrystals. Reactions performed near the isoelectric point of pH 6.7 have been shown to make micrometer sized particles with smaller particles being produced at slightly acidic or basic conditions.[27] Here, we have used a pH 9 solution to synthesize our nanocrystals. Basic conditions are also known to produce CuO and Cu_2O side products which must be removed by washing with NH_4OH.[8,10] The production of copper oxide side products in the synthesis could certainly account for a deficiency of copper atoms in $CuGaO_2$. The NH_4OH washing step may also be responsible for inducing copper vacancies postsynthesis by leaching copper atoms from edge sites of the nanocrystals. Studies investigating the dependence of copper vacancies on synthetic procedure are currently underway in our laboratory.

In the context of solar-to-electrical and solar-to-fuel energy conversion strategies, $CuGaO_2$ represents one of only a handful of p-type metal oxides able to serve as a hole transport layer.[4,14] It is therefore critical to further understand its band structure, density of defect states, and hole diffusion for the successful development of these technologies. Understanding the energy and density of valence band states can better direct the synthesis of light absorbing molecules to achieve higher injection yields of photogenerated holes, while understanding the exact nature of defect states in these materials can help decipher the effect they may have on electron−hole recombination at the $CuGaO_2$/solution interface or their role in hole transport through the material. Copper vacancies observed here were found to enhance the conductivity of $CuGaO_2$ films; however, they are also expected to act as recombination centers between photogenerated holes and electron donors, thus limiting solar energy conversion efficiency. For example, nickel vacancies in p-type NiO also display quasi-reversible redox features and passivation of these defects has led to improved device performance.[36,50] Passivation of copper vacancies in $CuGaO_2$ may offer a means of achieving large hole conductivities without surface recombination. Likewise, the synthesis of smaller, isotropic $CuGaO_2$ nanocrystals that do not preferentially stack could remove the need for large hole densities by taking advantage of faster hole diffusion through Cu^I layers.

CONCLUSIONS

Here we have shown evidence for copper vacancies and Cu^{II} surface defects in $CuGaO_2$ nanocrystals. The density of holes induced by copper vacancies is estimated as an upper limit of $n_{h+} \sim 10^{21}$ cm^{-3}. The impact of this high concentration of holes is manifested by large conductivites for hole diffusion measured by electrochemical impedance spectroscopy and the presence of Cu^{II} surface defects measured by X-ray photoelectron spectroscopy and cyclic voltammetry. Applications of $CuGaO_2$ nanocrystals as hole transport layers in a wide range of solar energy conversion strategies, including both solar-to-electrical and solar-to-fuel, is predicated on the ability to control this hole density. The origin of copper vacancies in the present study is proposed to be due to the basic pH conditions for the synthesis of $CuGaO_2$ nanocrystals which suggests the possibility of tuning the density of holes based on the synthetic conditions.

ASSOCIATED CONTENT

Supporting Information

The Supporting Information is available free of charge on the ACS Publications website at DOI: 10.1021/acsaem.8b01558.

EDS, powder XRD, ATR-IR, UV−vis−near-IR, XPS, CV, and EIS data (PDF)

AUTHOR INFORMATION

Corresponding Author

*E-mail: farnum@auburn.edu.

ORCID

Ryan B. Comes: 0000-0002-5304-6921

Byron H. Farnum: 0000-0001-9152-1909

DOI: 10.1021/acsaem.8b01558
ACS Appl. Energy Mater. 2019, 2, 19−28

Notes

The authors declare no competing financial interest.

■ ACKNOWLEDGMENTS

We acknowledge funding support from the National Science Foundation, Division of Materials Research and EPSCoR through Grant No. 1809847. We also acknowledge support from the Department of Chemistry and Biochemistry and Department of Physics at Auburn University.

■ REFERENCES

(1) Wang, J.; Ibarra, V.; Barrera, D.; Xu, L.; Lee, Y.-J.; Hsu, J. W. P. Solution Synthesized P-Type Copper Gallium Oxide Nanoplates as Hole Transport Layer for Organic Photovoltaic Devices. *J. Phys. Chem. Lett.* **2015**, *6*, 1071−1075.

(2) Renaud, A.; Cario, L.; Deniard, P.; Gautron, E.; Rocquefelte, X.; Pellegrin, Y.; Blart, E.; Odobel, F.; Jobic, S. Impact of Mg Doping on Performances of $CuGaO_2$ Based P-Type Dye-Sensitized Solar Cells. *J. Phys. Chem. C* **2014**, *118*, 54−59.

(3) Creissen, C. E.; Warnan, J.; Reisner, E. Solar H_2 Generation in Water with a $CuCrO_2$ Photocathode Modified with an Organic Dye and Molecular Ni Catalyst. *Chem. Sci.* **2018**, *9*, 1439−1447.

(4) Odobel, F.; Pellegrin, Y. Recent Advances in the Sensitization of Wide-Band-Gap Nanostructured P-Type Semiconductors. Photovoltaic and Photocatalytic Applications. *J. Phys. Chem. Lett.* **2013**, *4*, 2551−2564.

(5) Xiong, D.; Xu, Z.; Zeng, X.; Zhang, W.; Chen, W.; Xu, X.; Wang, M.; Cheng, Y.-B. Hydrothermal Synthesis of Ultrasmall $CuCrO_2$ Nanocrystal Alternatives to NiO Nanoparticles in Efficient P-Type Dye-Sensitized Solar Cells. *J. Mater. Chem.* **2012**, *22*, 24760−24768.

(6) Renaud, A.; Chavillon, B.; Le Pleux, L.; Pellegrin, Y.; Blart, E.; Boujtita, M.; Pauporté, T.; Cario, L.; Jobic, S.; Odobel, F. $CuGaO_2$: A Promising Alternative for NiO in p-Type Dye Solar Cells. *J. Mater. Chem.* **2012**, *22*, 14353−14356.

(7) Yu, M.; Natu, G.; Ji, Z.; Wu, Y. P-Type Dye-Sensitized Solar Cells Based on Delafossite $CuGaO_2$ Nanoplates with Saturation Photovoltages Exceeding 460 mV. *J. Phys. Chem. Lett.* **2012**, *3*, 1074−1078.

(8) Srinivasan, R.; Chavillon, B.; Doussier-Brochard, C.; Cario, L.; Paris, M.; Gautron, E.; Deniard, P.; Odobel, F.; Jobic, S. Tuning the Size and Color of the P-Type Wide Band Gap Delafossite Semiconductor $CuGaO_2$ with Ethylene Glycol Assisted Hydrothermal Synthesis. *J. Mater. Chem.* **2008**, *18*, 5647−5653.

(9) Kumagai, H.; Sahara, G.; Maeda, K.; Higashi, M.; Abe, R.; Ishitani, O. Hybrid Photocathode Consisting of a $CuGaO_2$ P-Type Semiconductor and a Ru(II)−Re(I) Supramolecular Photocatalyst: Non-Biased Visible-Light-Driven CO_2 Reduction with Water Oxidation. *Chem. Sci.* **2017**, *8*, 4242−4249.

(10) Xu, Z.; Xiong, D.; Wang, H.; Zhang, W.; Zeng, X.; Ming, L.; Chen, W.; Xu, X.; Cui, J.; Wang, M.; Powar, S.; Bach, U.; Cheng, Y.-B. Remarkable Photocurrent of p-Type Dye-Sensitized Solar Cell Achieved by Size Controlled $CuGaO_2$ Nanoplates. *J. Mater. Chem. A* **2014**, *2*, 2968−2976.

(11) Zhang, H.; Wang, H.; Chen, W.; Jen, A. K.-Y. $CuGaO_2$: A Promising Inorganic Hole-Transporting Material for Highly Efficient and Stable Perovskite Solar Cells. *Adv. Mater.* **2017**, *29*, 1604984.

(12) Xiong, D.; Zhang, W.; Zeng, X.; Xu, Z.; Chen, W.; Cui, J.; Wang, M.; Sun, L.; Cheng, Y.-B. Enhanced Performance of P-Type Dye-Sensitized Solar Cells Based on Ultrasmall Mg-Doped $CuCrO_2$ Nanocrystals. *ChemSusChem* **2013**, *6*, 1432−1437.

(13) Wang, J.; Lee, Y.-J.; Hsu, J. W. P. Sub-10 Nm Copper Chromium Oxide Nanocrystals as a Solution Processed P-Type Hole Transport Layer for Organic Photovoltaics. *J. Mater. Chem. C* **2016**, *4*, 3607−3613.

(14) Yu, M.; Draskovic, T. I.; Wu, Y. Cu(I)-Based Delafossite Compounds as Photocathodes in p-Type Dye-Sensitized Solar Cells. *Phys. Chem. Chem. Phys.* **2014**, *16*, 5026−5033.

(15) Draskovic, T. I.; Yu, M.; Wu, Y. 2H-$CuScO_2$ Prepared by Low-Temperature Hydrothermal Methods and Post-Annealing Effects on Optical and Photoelectrochemical Properties. *Inorg. Chem.* **2015**, *54*, 5519−5526.

(16) Lekse, J. W.; Underwood, M. K.; Lewis, J. P.; Matranga, C. Synthesis, Characterization, Electronic Structure, and Photocatalytic Behavior of $CuGaO_2$ and $CuGa_{1-x}Fe_xO_2$ (X = 0.05, 0.10, 0.15, 0.20) Delafossites. *J. Phys. Chem. C* **2012**, *116*, 1865−1872.

(17) Jang, Y. J.; Park, Y. B.; Kim, H. E.; Choi, Y. H.; Choi, S. H.; Lee, J. S. Oxygen-Intercalated $CuFeO_2$ Photocathode Fabricated by Hybrid Microwave Annealing for Efficient Solar Hydrogen Production. *Chem. Mater.* **2016**, *28*, 6054−6061.

(18) Prévot, M. S.; Jeanbourquin, X. A.; Bourée, W. S.; Abdi, F.; Friedrich, D.; van de Krol, R.; Guijarro, N.; Le Formal, F.; Sivula, K. Evaluating Charge Carrier Transport and Surface States in $CuFeO_2$ Photocathodes. *Chem. Mater.* **2017**, *29*, 4952−4962.

(19) Gu, J.; Yan, Y.; Krizan, J. W.; Gibson, Q. D.; Detweiler, Z. M.; Cava, R. J.; Bocarsly, A. B. P-Type $CuRhO_2$ as a Self-Healing Photoelectrode for Water Reduction under Visible Light. *J. Am. Chem. Soc.* **2014**, *136*, 830−833.

(20) Gu, J.; Wuttig, A.; Krizan, J. W.; Hu, Y.; Detweiler, Z. M.; Cava, R. J.; Bocarsly, A. B. Mg-Doped $CuFeO_2$ Photocathodes for Photoelectrochemical Reduction of Carbon Dioxide. *J. Phys. Chem. C* **2013**, *117*, 12415−12422.

(21) Read, C. G.; Park, Y.; Choi, K.-S. Electrochemical Synthesis of P-Type $CuFeO_2$ Electrodes for Use in a Photoelectrochemical Cell. *J. Phys. Chem. Lett.* **2012**, *3*, 1872−1876.

(22) Toyoda, K.; Hinogami, R.; Miyata, N.; Aizawa, M. Calculated Descriptors of Catalytic Activity for Water Electrolysis Anode: Application to Delafossite Oxides. *J. Phys. Chem. C* **2015**, *119*, 6495−6501.

(23) Kawazoe, H.; Yasukawa, M.; Hyodo, H.; Kurita, M.; Yanagi, H.; Hosono, H. P-Type Electrical Conduction in Transparent Thin Films of $CuAlO_2$. *Nature* **1997**, *389*, 939−942.

(24) Tate, J.; Ju, H. L.; Moon, J. C.; Zakutayev, A.; Richard, A. P.; Russell, J.; McIntyre, D. H. Origin of p-Type Conduction in Single-Crystal $CuAlO_2$. *Phys. Rev. B: Condens. Matter Mater. Phys.* **2009**, *80*, 165206.

(25) Herraiz-Cardona, I.; Fabregat-Santiago, F.; Renaud, A.; Julián-López, B.; Odobel, F.; Cario, L.; Jobic, S.; Giménez, S. Hole Conductivity and Acceptor Density of P-Type $CuGaO_2$ Nanoparticles Determined by Impedance Spectroscopy: The Effect of Mg Doping. *Electrochim. Acta* **2013**, *113*, 570−574.

(26) Sheets, W. C.; Mugnier, E.; Barnabé, A.; Marks, T. J.; Poeppelmeier, K. R. Hydrothermal Synthesis of Delafossite-Type Oxides. *Chem. Mater.* **2006**, *18*, 7−20.

(27) Yu, M.; Draskovic, T. I.; Wu, Y. Understanding the Crystallization Mechanism of Delafossite $CuGaO_2$ for Controlled Hydrothermal Synthesis of Nanoparticles and Nanoplates. *Inorg. Chem.* **2014**, *53*, 5845−5851.

(28) Ueda, K.; Hase, T.; Yanagi, H.; Kawazoe, H.; Hosono, H.; Ohta, H.; Orita, M.; Hirano, M. Epitaxial Growth of Transparent P-Type Conducting $CuGaO_2$ Thin Films on Sapphire (001) Substrates by Pulsed Laser Deposition. *J. Appl. Phys.* **2001**, *89*, 1790−1793.

(29) Wang, C.; Li, Q.; Wang, F.; Xia, G.; Liu, R.; Li, D.; Li, N.; Spendelow, J. S.; Wu, G. Morphology-Dependent Performance of CuO Anodes via Facile and Controllable Synthesis for Lithium-Ion Batteries. *ACS Appl. Mater. Interfaces* **2014**, *6*, 1243−1250.

(30) Chen, K.; Song, S.; Li, K.; Xue, D. Water-Soluble Inorganic Salts with Ultrahigh Specific Capacitance: Crystallization Transformation Investigation of $CuCl_2$ Electrodes. *CrystEngComm* **2013**, *15*, 10367−10373.

(31) Lu, Y.; Yan, H.; Qiu, K.; Cheng, J.; Wang, W.; Liu, X.; Tang, C.; Kim, J.-K.; Luo, Y. Hierarchical Porous CuO Nanostructures with Tunable Properties for High Performance Supercapacitors. *RSC Adv.* **2015**, *5*, 10773−10781.

(32) Bard, A. J.; Faulkner, L. R. *Electrochemical Methods: Fundamentals and Applications*; Wiley: New York, 1980.

DOI: 10.1021/acsaem.8b01558
ACS Appl. Energy Mater. 2019, 2, 19−28

(33) Fabregat-Santiago, F.; Garcia-Belmonte, G.; Bisquert, J.; Zaban, A.; Salvador, P. Decoupling of Transport, Charge Storage, and Interfacial Charge Transfer in the Nanocrystalline TiO_2/Electrolyte System by Impedance Methods. *J. Phys. Chem. B* **2002**, *106*, 334−339.
(34) Bisquert, J. Theory of the Impedance of Electron Diffusion and Recombination in a Thin Layer. *J. Phys. Chem. B* **2002**, *106*, 325−333.
(35) Shi, L.; Wang, F.; Wang, Y.; Wang, D.; Zhao, B.; Zhang, L.; Zhao, D.; Shen, D. Photoluminescence and Photocatalytic Properties of Rhombohedral $CuGaO_2$ Nanoplates. *Sci. Rep.* **2016**, *6*, 21135.
(36) Flynn, C. J.; McCullough, S. M.; Oh, E.; Li, L.; Mercado, C. C.; Farnum, B. H.; Li, W.; Donley, C. L.; You, W.; Nozik, A. J.; McBride, J. R.; Meyer, T. J.; Kanai, Y.; Cahoon, J. F. Site-Selective Passivation of Defects in NiO Solar Photocathodes by Targeted Atomic Deposition. *ACS Appl. Mater. Interfaces* **2016**, *8*, 4754−4761.
(37) Meyer, G. J. Molecular Approaches to Solar Energy Conversion with Coordination Compounds Anchored to Semiconductor Surfaces. *Inorg. Chem.* **2005**, *44*, 6852−6864.
(38) Flynn, C. J.; Oh, E. E.; McCullough, S. M.; Call, R. W.; Donley, C. L.; Lopez, R.; Cahoon, J. F. Hierarchically-Structured NiO Nanoplatelets as Mesoscale P-Type Photocathodes for Dye-Sensitized Solar Cells. *J. Phys. Chem. C* **2014**, *118*, 14177−14184.
(39) Ingram, B. J.; Harder, B. J.; Hrabe, N. W.; Mason, T. O.; Poeppelmeier, K. R. Transport and Defect Mechanisms in Cuprous Delafossites. 2. $CuScO_2$ and $CuYO_2$. *Chem. Mater.* **2004**, *16*, 5623−5629.
(40) Robertson, J.; Clark, S. J. Limits to Doping in Oxides. *Phys. Rev. B: Condens. Matter Mater. Phys.* **2011**, *83*, 075205.
(41) Scanlon, D. O.; Watson, G. W. Conductivity Limits in $CuAlO_2$ from Screened-Hybrid Density Functional Theory. *J. Phys. Chem. Lett.* **2010**, *1*, 3195−3199.
(42) Isawa, K.; Yaegashi, Y.; Komatsu, M.; Nagano, M.; Sudo, S.; Karppinen, M.; Yamauchi, H. Synthesis of Delafossite-Derived Phases, $RCuO_{2+\delta}$ with R = Y, La, Pr, Nd, Sm, and Eu, and Observation of Spin-Gap-like Behavior. *Phys. Rev. B: Condens. Matter Mater. Phys.* **1997**, *56*, 3457−3466.
(43) Cava, R. J.; Zandbergen, H. W.; Ramirez, A. P.; Takagi, H.; Chen, C. T.; Krajewski, J. J.; Peck, W. F.; Waszczak, J. V.; Meigs, G.; Roth, R. S.; Schneemeyer, L. F. $LaCuO_{2.5+x}$ and $YCuO_{2.5+x}$Delafossites: Materials with Triangular $Cu^{2+\delta}$Planes. *J. Solid State Chem.* **1993**, *104*, 437−452.
(44) Garlea, O.; Darie, C.; Bougerol, C.; Isnard, O.; Bordet, P. Structure of $LaCuO_{2.66}$An Oxidized Delafossite Compound Containing Hole-Doped Kagome Planes of Cu^{2+} Cations. *Solid State Sci.* **2003**, *5*, 1095−1104.
(45) Ingram, B. J.; González, G. B.; Mason, T. O.; Shahriari, D. Y.; Barnabè, A.; Ko, D.; Poeppelmeier, K. R. Transport and Defect Mechanisms in Cuprous Delafossites. 1. Comparison of Hydrothermal and Standard Solid-State Synthesis in $CuAlO_2$. *Chem. Mater.* **2004**, *16*, 5616−5622.
(46) Hamberg, I.; Granqvist, C. G. Evaporated Sn-doped In_2O_3 Films: Basic Optical Properties and Applications to Energy-efficient Windows. *J. Appl. Phys.* **1986**, *60*, R123−R160.
(47) Han, M.; Jiang, K.; Zhang, J.; Yu, W.; Li, Y.; Hu, Z.; Chu, J. Structural, Electronic Band Transition and Optoelectronic Properties of Delafossite $CuGa_{1-x}Cr_xO_2$ ($0 \leq X \leq 1$) Solid Solution Films Grown by the Sol−gel Method. *J. Mater. Chem.* **2012**, *22*, 18463−18470.
(48) Kawazoe, H.; Yasukawa, M.; Hyodo, H.; Kurita, M.; Yanagi, H.; Hosono, H. P-Type Electrical Conduction in Transparent Thin Films of $CuAlO_2$. *Nature* **1997**, *389*, 939−942.
(49) Pavlishchuk, V. V.; Addison, A. W. Conversion Constants for Redox Potentials Measured versus Different Reference Electrodes in Acetonitrile Solutions at 25°C. *Inorg. Chim. Acta* **2000**, *298*, 97−102.
(50) Flynn, C. J.; McCullough, S. M.; Li, L.; Donley, C. L.; Kanai, Y.; Cahoon, J. F. Passivation of Nickel Vacancy Defects in Nickel Oxide Solar Cells by Targeted Atomic Deposition of Boron. *J. Phys. Chem. C* **2016**, *120*, 16568−16576.

DOI: 10.1021/acsaem.8b01558
ACS Appl. Energy Mater. 2019, 2, 19−28